This item is the archived peer-reviewed author-version of:

Hierarchically dual-mesoporous TiO_2 microspheres for enhanced photocatalytic properties and lithium storage

Accepted Article

Authors: Sa Xiao, Yi Lu, Xin Li, Bing-Yu Xiao, Liang Wu, Jian-Ping Song, Yu-Xuan Xiao, Si-Ming Wu, Jie Hu, Yong Wang, Gang-Gang Chang, Ge Tian, Silvia Lenaerts, Christoph Janiak, Xiao-Yu Yang, and Bao-Lian Su

WILEY-VCH

Hierarchically Dual-mesoporous TiO₂ Microspheres for Enhanced Photocatalytic Properties and Lithium Storage

Sa Xiao,[a] Yi Lu,[a] Xin Li,[a] Bing-Yu Xiao,[a] Liang Wu,[a] Jian-Ping Song,[a] Yu-Xuan Xiao,[a] Si-Ming Wu,[a] Jie Hu,[a] Yong Wang,[a] Gang-Gang Chang,[a] Ge Tian,*[a] Silvia Lenaerts,[b] Christoph Janiak,[c] Xiao-Yu Yang*[a, d] and Bao-Lian Su[a, e]

Abstract: Hierarchically dual-mesoporous TiO₂ microspheres have been synthesized via a solvothermal process in the presence of 1-butyl-3–methylmidazolium tetrafluoroborate ([BMIm][BF₄]) and diethylenetriamine (DETA) as co-templates. Secondary mesostructured defects in the hierarchical TiO₂ microspheres produce the oxygen vacancies, which not only significantly enhance the photocatalytic activity on degrading methyl blue (over 1.7 times to P25) and acetone (over 2.9 times of P25), but which also are beneficial for lithium storage. Moreover, we propose a mechanism to obtain a better understanding of the role of dual mesoporosity of TiO₂ microspheres for enhancing the molecular diffusion, ion transportation and electron transformation.

Introduction

Mesoporous semiconductors enhance catalysis, photocatalysis and electrical energy storage because the meso-structure provides the desired highly accessible surface area, uniform porous structure and an adjustable open framework.[1-10] Hierarchically mesoporous TiO₂ microspheres are therefore of great interest for high-performance photocatalysts [11-13] and high-energy-storage host-materials [14], because hierarchical structures may exhibit very interesting properties, such as edge-active sites, unique multi-dimensional morphology, a

[a]   S. Xiao, Y. Lu, X. Li, B.-Y. Xiao, L. Wu, J.-P. Song, Y.-X. Xiao,
       S.-M. Wu, J. Hu, Y. Wang, Prof. G.-G. Chang, Prof. G. Tian,
       Prof. X.-Y. Yang, Prof. B.-L. Su
       State Key Laboratory Advanced Technology for Materials
       Synthesis and Processing and School of Material Science &
       Engnineering
       Wuhan University of Technology
       122, Luoshi Road, Wuhan, 430070, China.
       E-mail: tiange@whut.edu.cn, xyyang@whut.edu.cn
[b]   Prof. S. Lenaerts
       Research Group of Sustainable Energy and Air Purification
       (DuEL), Department of Bioscience Engineering
       University of Antwerp
       Antwerp, Belgium
[c]   Prof. C. Janiak
       Institut für Anorganische Chemie und Strukturchemie
       Heinrich-Heine-Universität Düsseldorf
       40204 Düsseldorf, Germany
[d]   Dr. X.-Y. Yang
       School of Engineering and Applied Sciences,
       Harvard University,
       Cambridge, Massachusetts 02138, USA
       E-mail: xyyang@seas.harvard.edu
[e]   Prof. B.-L. Su
       Laboratory of Inorganic Materials Chemistry (CMI)
       University of Namur
       61, rue de Bruxelles, 5000 Namur, Belgium
       E-mail: bao-lian.su@fundp.ac.be
       Supporting information for this article is given via a link at the end
    of the document.

combination of micro-nano scales, shortened diffusion paths and a larger contact area.[15-17] Monodispersed spherical TiO₂ structures can be successfully obtained by sol-gel methods by controlling the hydrolysis-condensation and the crystallization temperature.[18-21] However, many critical issues need to be addressed, such as the poor porous structure, the random crystal fusion and the number of grain boundaries. This often results in a low level of active defects and a fast loss of electrons due to recombination or back-reaction. Oriented nanostructured TiO₂ such as nanocrystals[18, 22] and nanosheets[19, 23, 24] have been subsequently developed to improve the photocatalytic activity and/or energy storage capacity, owing to an enhancement of the charges transport and interparticles connection. Great progress has been made to design mesoporous single-crystal TiO₂, which leads to enhanced mobility and photoelectronic performance.[1] However, as a result of the large-scale and highly crystalline TiO₂, it seems inevitable to expect a decrease of the surface defects/sites[25] and an unavailability of inner crystal lattices[26].

Recently it was found that defect sites are of key importance to tune the functional properties of metal oxides, such as their electronic structure, charge transport, and catalytic performance.[22] Metal and oxygen vacancies are thought to be very important for engineering predictable semiconductors with remarkable properties. For example, substitutional impurities, including metal ions and doping atoms (such as H, N, F), have been used to replace oxygen in order to generate oxygen site vacancies. Physical treatments such as high-energy irradiation or oxygen-poor and oxygen-rich treatment have also been effective to introduce oxygen/metal vacancies.[27-28] However, there are only rare reports on nanosized defects because the generation of nanoscale vacancies in single crystals is more difficult than atom-level defects.

Ionic liquids (ILs) were developed as templates because of their unique templating behavior, based on the distinct polarizability of the head groups, leading to highly ordered pore systems.[29,30] In particular, ILs as environmentally benign nonvolatile and thermally stable organic co-templates,[25] showing a significantly stronger tendency toward self-aggregation and tolerance toward perturbations with other templates, have been reported to synthesize hierarchical dual-mesoporous materials.[31,32] BF₄ anions in ILs (designed as IL-F) can interact with Ti cations because of a high F···Ti bonding energy, and act as templates to form a pore and/or defect structure at a nanoscale. At the same time, decomposition and ready hydrolysis of BF_4^- will yield F⁻ anions to yield Ti···F atom level defects.

Here we report a one-pot synthesis of hierarchically dual-mesoporous TiO₂ microspheres (HDM-TiO₂) via a solvothermal process in the presence of 1-butyl-3–methylimidazolium tetrafluoroborate ([BMIm][BF₄]) and diethylenetriamine (DETA)

as co-templates. This dual mesoporosity of the HDM-TiO₂ microspheres plays an important role to enhance molecule diffusion, ion transportation and electron transformation, which can greatly improve both the photocatalytic properties and the capacity for lithium storage.
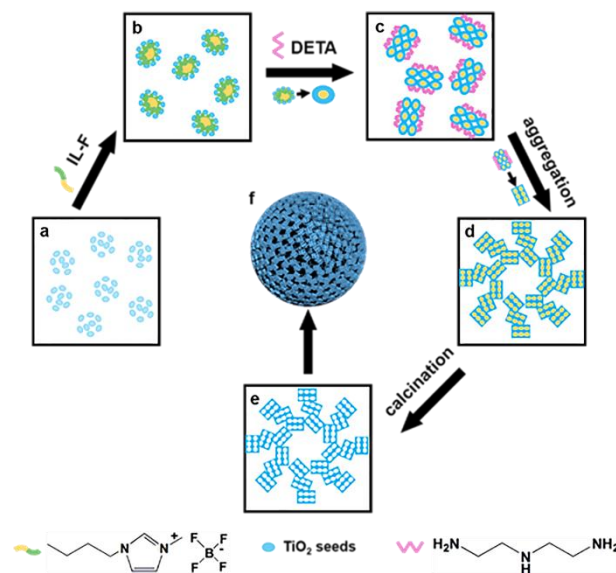
Results and Discussion

Figure 1. Schematic representation of the formation mechanism of HDM-TiO₂: a cooperative self-assembly process in the presence of 1-butyl-3–methylimidazolium tetrafluoroborate ([BMIm][BF₄]) and DETA as the structure-directing agent stand for the five procedures and its final 3D stucture: (a), TiO₂ seeds from titanium precursor, (b) TiO₂-IL oligomers after adding the IL, (c) TiO₂ nanoparticles formation caused by DETA, (d) TiO₂ microspheres formation via nanoparticles self-assembly, (e) hierarchically dual-mesoporous TiO₂ microspheres by calcination and (f) corresponding 3D model.

Figure 1 illustrates the fabrication process of HDM-TiO₂ and demonstrates the proposed mechanism of the formed morphology by [BMIm][BF₄] and DETA during the solvothermal synthesis procedure. The TiO₂ precursor (Figure 1a) is first mixed with the [BMIm][BF₄] to form TiO₂-IL oligomers (Figure 1b), because of the high F···Ti interaction energy and the templating effect of IL.[26,33] During the solvothermal (propanol) process, TiO₂-IL oligomers are effectively controlled to grow along the [001] direction by DETA stabilization and aggregate to nanoparticles (Figure 1c).[19] Because the Ti···F bonds are stronger than the Ti···N bonds, the TiO₂ nanoparticles contain and bind the [BMIm][BF₄] template.[26] These nanoparticles are highly flexible and easily self-organize into hierarchical spheres (Figure 1d). After calcination at 600 °C for 4 h, [BMIm][BF₄] and DETA are removed (Figure 1e) and finally we obtain the hierarchically dual-mesoporous structure (Figure 1f).

The morphology and structure of HDM-TiO₂ is characterized by STEM and HAADF-TEM (Figure 2). The STEM image of HDM-TiO₂ in Figure 2a indicates that the microsphere is built up by TiO₂ nanoparticles. The TEM image from the HDM-TiO₂ microsphere (Figure 2b) shows that the length of nanoparticles ranges from 15 nm to 25 nm and that there are large-size

mesopores caused by the aggregation of these nanoparticles. The TiO₂ nanoparticles are bound together by an interconnecting amorphous/semi-crystalline interface; and this hetero-phase is heterogeneous and coherent on an atomic scale (Figure 2c). The 0.23 nm lattice spacing of the facets in Figure 2d, points to the (001) interplanar distance of TiO₂. The HRTEM image (Figure 2e) and the inverse FFT (Figure 2f) of a single nanoparticle show that there are secondary mesopores with a size of around 4 nm within the single crystal nanoparticles. These mesopores randomly disperse within the nanoparticles and show a hexagonal defect configuration (Figure 2e and 2f); these inner mesopores have no influence on the single crystal structure. The Ti···F of TiO₂-IL oligomers normally link with neighboring Ti-O bonds for crystal growth, which can remain the single crystal structure of nanoparticles, and the IL fragments of TiO₂-IL oligomers act as templates to form the nanoscale defect.
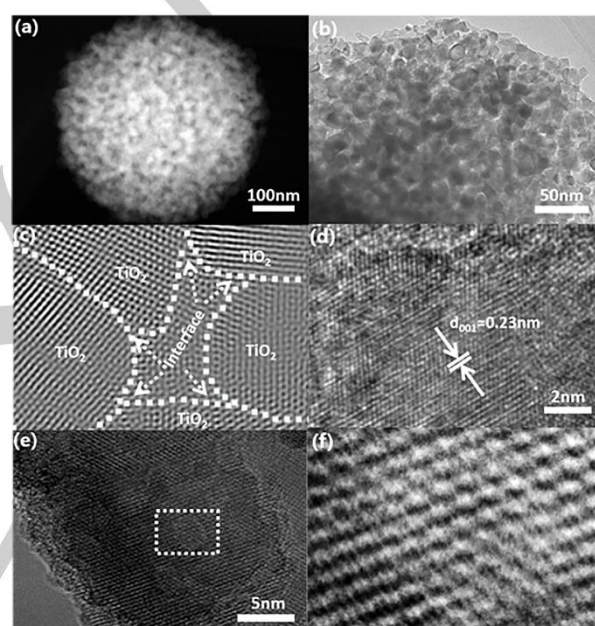

Figure 2. STEM image (a) and HRTEM image (b) of HDM-TiO₂, inversed FFT pattern (c) of HDM-TiO₂ (fig. S1e), where the dotted lines indicate the boundary of the nanoparticles of HDM-TiO₂ HRTEM (d) of some nanoparticles of HDM-TiO₂, HR-TEM (e, the inner hexagons represent the mesopores) of a nanoparticle of HDM-TiO₂, inverse FFT pattern (f) of HDM-TiO₂ (e).

HDM-TiO₂ and the samples for comparison (as-synthesized HDM TiO₂, and as-synthesized and calcined TiO₂ without using IL-F as template, termed HM-TiO₂) have also been characterized. The XRD patterns (Figure S2) show that all samples match well with the standard PDF CARDS (010-078-2486) of anatase TiO₂. Note that the XRD peaks of HDM-TiO₂ are sharper and narrower than the one of HM-TiO₂, indicating that the crystallization of HDM-TiO₂ is enhanced. Figure S3 shows the nitrogen adsorption-desorption isotherms and the pore size distribution curves (inset) of as-synthesized and calcined HDM-TiO₂ and HM-TiO₂. The inset in Figure S3 and Table S1 shows that before calcination the single pore distributions of HDM-TiO₂ and HM-TiO₂ are around 12 nm and 7 nm, respectively. After calcination HDM-TiO₂ shows a dual pore size distribution (around 4 nm and 20 nm), due to the removal of

the IL-F templating; this is also in good accord with the TEM data. Moreover, after calcination, the specific surface area of HDM-TiO$_2$ shows a big increase from 84 m^{2}g^{-1} to 131 m^{2}g^{-1}, compared to the decrease of HM-TiO$_2$ (from 86 m^{2}g^{-1} to 57 m^{2}g^{-1}), because of the secondary mesopores. The SAXS patterns of HDM-TiO$_2$ and HM-TiO$_2$ prepared at as-synthesized and calcined for 600°C are collected in Figure S4. All of the samples have a broad peak in low q values (q=4πsinh/λ), indicating the defined mesostructures.[34] After calcination, the peaks of HDM-TiO$_2$ and HM-TiO$_2$ shift to lower q values and the unit cell parameter (a$_0$) is respectively changed from 25.6 to 28.3 nm and 22.8 to 24.3 nm, which is coincident with the BET results. Figure S5 displays Raman spectra of HDM-TiO$_2$, HM-TiO$_2$ and P25, five Raman active modes of Eg (146 cm^{-1}), Eg (198 cm^{-1}), B$_1$g (399 cm^{-1}), A$_1$g (519 cm^{-1}) and Eg (641 cm^{-1}) are observed. This result clearly indicates that the well-crystallized structure is preserved in the solvothermal synthesis. Figure S6 indicates FT-IR spectra of HDM-TiO$_2$ and HM-TiO$_2$, the broad absorption peaks at 3430 cm^{-1} and 1620 cm^{-1} are attributed to the stretching and bending vibration of surface absorbed water and hydroxyl groups, respectively. HDM-TiO$_2$ has stronger peaks at 3430 cm^{-1} and 1620 cm^{-1}, indicated that HDM-TiO$_2$ has more Ti-OH bonds and is easier to degrade organic compounds.[35] The absorption at around 510 cm^{-1} is assigned to the stretching vibration of Ti-O-Ti. The PL spectra of HDM-TiO$_2$, HM-TiO$_2$ and P25 in the wavelength range of 350–550 nm with the excitation light at 320 nm is recorded in Figure S7. All the samples have five peaks and HDM-TiO$_2$ has the lowest peak among three samples.[36] This observation indicates that the HDM-TiO$_2$ with dual-mesoporous structure has a relatively low recombination rate of electrons and holes, which leads to high photocatalytic activity. Figure S8 shows TGA curve of HDM-TiO$_2$ and HM-TiO$_2$ under an air flow at a temperature ramp of 5 °C min^{-1}. HM-TiO$_2$ mainly has two processes of weight loss, the first is the absorption and bound of water under 280 °C, the second weight loss is the loss of organics and the transformation of crystalline between 280 °C to 600 °C. While HDM-TiO$_2$ has a fast falling between 480 °C to 600 °C owing to the removal of IL. With the removal of IL at 600 °C, the secondary defected mesopores are formatted.

The photodegradation of methylene blue (MB) under full light irradiation is investigated to evaluate the photocatalytic activity of HDM-TiO$_2$, HM-TiO$_2$ and P25 in Figure 3a. Observing the degradation rate constant in Figure 3a, it is very clear that the HDM-TiO$_2$ exhibits the highest photocatalytic activity with a rate constant of 1.54×10^{-3} min^{-1}, which is about 1.7 times that of P25 (9.3×10^{-4} min^{-1}) and 3.3 times that of HM-TiO$_2$ (4.6×10^{-4} min^{-1}). Figure 3b displays the concentration of acetone under irradiation in the presence of HDM-TiO$_2$, HM-TiO$_2$ and P25. As is shown on degrading MB, HDM-TiO$_2$ also shows the highest photocatalytic activity with a rate constant of 9.68×10^{-3} min^{-1}; almost 2.9 times of P25 (3.41×10^{-3} min^{-1}) and 2.3 times that of HM-TiO$_2$ (4.2×10^{-3} min^{-1}). HDM-TiO$_2$ exhibits a higher photocatalytic activity both on degrading MB and acetone than HM-TiO$_2$ (single porosity) owing to its unique hierarchically dual mesoporosity where the primary large-size mesopores increase the contact area between the dyes with HDM-TiO$_2$ and avail the diffusion and transport of the dye in HDM-TiO$_2$, while the secondary small-sized mesopores induce more defects and active sites. Compared with MB, acetone is smaller and more accessible to diffuse into the secondary porosity, so the acetone photodegradation of HDM-

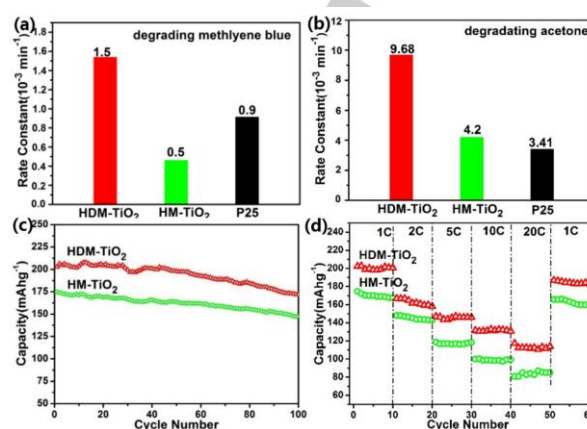TiO$_2$ and HM-TiO$_2$, both having mesoporosity, exhibit better properties than nanosized P25.

Figure 3. The photocatalytic rate constant of methylene blue (a) and acetone (b) with HDM-TiO$_2$, HM-TiO$_2$ and Degussa P25 under full light irradiation. Cycle performance of HDM-TiO$_2$ and HM-TiO$_2$ at a current density of 1 C (c) and various current rates of 1 C, 2 C,5 C, 10 C, 20 C and 1 C (d).

Figure 3c displays the high reversibility of the underlying electrochemical reactions over many charge-discharge cycles for HDM-TiO$_2$ and HM-TiO$_2$. Remarkably, at a rate of 1 C, HDM-TiO$_2$ still retains an average capacity of 188 mAhg^{-1} after 100 charge-discharge cycles. The rate performances of HDM-TiO$_2$ and HM-TiO$_2$ at the current rates of 1-20 C are compared in Figure 3d. Notably, the reversible capacities of HDM-TiO$_2$ are maintained at 202 and 130 mAhg^{-1} at 1 C and 10 C, respectively. Even at a high current rate of 20 C, a high capacity of 125 mAhg^{-1} could still be obtained, showing a magnificent high-rate performance. Moreover, a capacity of 186 mAhg^{-1} is maintained when the rate is turned back to 1 C. The cyclic voltammograms (CVs) of HDM-TiO$_2$ shown in Figure S9a display two well-defined current peaks corresponding to lithium insertion and extraction at the potential of 1.7 V (Li-insertion) and 2.1 V (Li-extraction). And the second and the third CV curves almost overlap with the first one, suggesting the high reversibility and stability of the electrode in the following sweeps. Figure S9b presents the discharge-charge curves of HDM-TiO$_2$ at 1st, 2nd, 10th and 100th cycles at 1 C (170 mAg^{-1}). It is evident that HDM-TiO$_2$ exhibits well-defined voltage plateaus, which can be observed at 1.7 V and 2.1 V during lithium ion discharge and charge, which are in accordance with the CV curves. Fig. S9c further displays the cycle performance of HDM-TiO$_2$ and HM-TiO$_2$ at 2 C and 5 C, respectively. Remarkably, HDM-TiO$_2$ retains both high average capacities of 160 and 132 mAhg^{-1} after 100 cycles at the rate of 2 C and 5 C, while the HM-TiO$_2$ only has an average capacity of 136 and 104 mAhg^{-1}, respectively. Figure S9d exhibits electrochemical impedance spectroscopy (EIS) analyses of HDM-TiO$_2$ and HM-TiO$_2$. Nyquist plots are composed of a depressed semicircle (high-frequency region) and an inclined line (low-frequency region). The high frequency region of the semicircle is a measure of the charge-transfer impedance (R$_{ct}$). HDM-TiO$_2$ electrode demonstrates R$_{ct}$ value of 33 Ω and lower than HM-TiO$_2$ (72 Ω), due to its higher level of the oxygen vacancies. Therefore, HDM-TiO$_2$ shows a

better performance on lithium storage than HM-TiO$_2$, because HDM-TiO$_2$ has dual mesopores with large pores and nanoscale defects which decrease the diffusion distance of Li$^+$ and promote Li$^+$ insertion /desertion.

To get more information about the defects of HDM-TiO$_2$, Electron paramagnetic resonance (EPR) spectra are recorded at room temperature in Figure 4a. The EPR signal of Ti^{3+}, O^{2-} and oxygen vacancies (VO) locate at g = 1.960-1.990, 2.020 and 2.003, respectively.[37] As shown in Figure 4a, the EPR peaks around g = 1.986 and 2.011 in HDM-TiO$_2$ present the signal of Ti^{3+} defects and oxygen vacancies respectively, while there is no peak in HM-TiO$_2$. It indicated that the defect structure is caused by the secondary mesopores, which is also in good accord with the defect structure shown in TEM images. In HDM-TiO$_2$, Ti^{3+} is produced by the existence of Ti-F-Ti bonds. As shown in Figure S10a and S10c, Ti^{4+} peaks in the Ti 2p spectra for HDM-TiO$_2$ are found at 459.1 and 464.7 eV, attributed to the Ti 2p3/2 and Ti 2p1/2 peaks. There is no detectable Ti^{3+} at the surface of all samples, probably due to the fact that Ti^{3+} is easily oxidized by a proper oxidant such as air-O$_2$ and/or water-dissolved O$_2$.[36] Compared to a typical Ti-O-Ti peak at 529.8 eV for HM-TiO$_2$ in Figure S10d, HDM-TiO$_2$ shows an extra O 1s peak at 531.8 eV, which is attributed to Ti-OH in Figure S10b. In addition, F1s XPS data of HDM-TiO$_2$ as-synthesized and calcined at 600 °C are shown in Figure S10e and S10f. There is a clear F1s (Figure S10e) peak at 684.1 eV in as-synthesized HDM-TiO$_2$ before calcination, which assigned to a typical F species such as in a Ti-F bond.[36] Then, after calcination, F species (Figure S10f) are removed and the peak disappears, which is in good agreement with the TGA data (Figure S8). The stronger oxygen vacancy signal is in good agreement with the EPR analysis. It reveals that HDM-TiO$_2$ has more oxygen vacancies than HM-TiO$_2$. With the removal of F and the escape of O atoms, more oxygen vacancies appears. To measure the photocatalytic activity, the photo-electrochemical (PEC) reaction is displayed in Figure 4b for HDM-TiO$_2$ and HM-TiO$_2$. The photocurrent density measured at 0.5 V (vs. Ag/AgCl) for HDM-TiO$_2$ (1.5 mA·cm^{-2}) is found to be 2.5 times that of HM-TiO$_2$ (0.94 mA·cm^{-2}). The high photocurrent density observed for HDM-TiO$_2$ is attributed to the existence of more oxygen vacancies. This indicates that introducing defect states can be very beneficial to separate of carriers and slightly decrease the conduction band of TiO$_2$ (Figure S11 and Table. S1).[38]
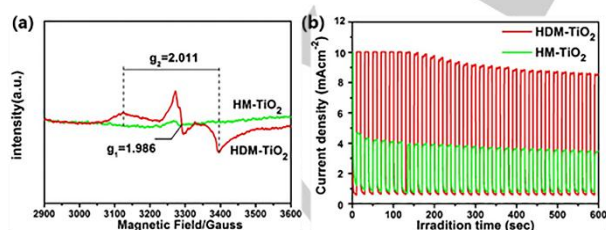

Figure 4. EPR spectra (a) and photoelectrochemical (PEC) reaction (b) of HDM-TiO$_2$ and HM-TiO$_2$.

Figure 5 shows the proposed mechanism of the photocatalytic degradation of MB and acetone and lithium storage in HDM-TiO$_2$. The nanoscale defect structure directly results in the presence of oxygen vacancies, which influence and slightly decrease the

band gap of HDM-TiO$_2$ (core part of Figure 5). Electrons can transfer from both the valence band and oxygen vacancies state to the conduction band of HDM-TiO$_2$.[38] This will be beneficial to both photogeneration electron transformation during photocatalysis and high electron conduction during insertion/desertion of lithium ions. The left of Figure5 (light blue area) shows the performance of HDM-TiO$_2$ on degrading acetone and MB. With the response of HDM-TiO$_2$ under UV light excitation, electrons can easily leap from both valence band and oxygen vacancies to the conduction band, and the "free" electrons in the defective crystal may take the place occupied by the O^{2-} anions in the regular lattice.[27] So such a way to generate photoelectrons would be avail to form holes, which can transfer H$_2$O and OH$^-$ to form the high reactive •OH and then degrade dye molecules. In our case, the large-sized pores in HDM-TiO$_2$ promote dye molecule diffusion between the TiO$_2$ nanoparticles and enhance contact and reaction area. The secondary defects in the TiO$_2$ nanoparticles not only enlarge the contact area, but also provide more oxygen vacancies, which accelerate electrons transfer effectively and enhance the photocatalytic activity. The lithium ion storage mechanism of HDM-TiO$_2$ is illustrated in the right part of Figure 5 (dark blue area). Similar to the dye molecule diffusion, the dual porous
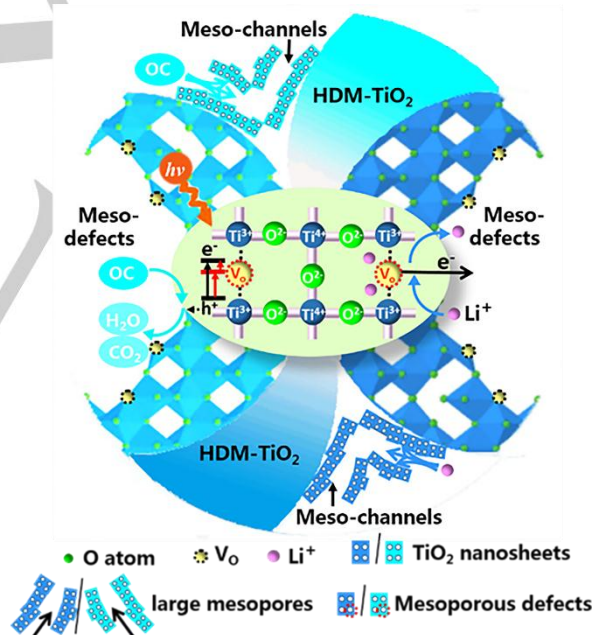

Figure 5. The mechanism of the OC (organic compounds including photocatalytic MB and acetone) degradation reaction (left) and lithium ions storage (right) in HDM-TiO$_2$. The light blue part in the left and the dark blue part in the right are mechanism of photocatalytic performance and lithium storage separately; the core part stands the ball-and-stick model of oxygen vacancies and Ti^{3+}.

structure can cut the diffusion distance of the electrolyte, which is avail to the insertion of lithium ions and the conduction of electrons. Moreover, oxygen vacancies caused by the

FULL PAPER

secondary porosity can enhance the electric conductivity, and significantly accelerate electron transfer, boost uptake and release of Li ions.

Conclusions

In summary, a facile co-templating approach to obtain hierarchically dual-mesoporous TiO_2 microspheres is presented. The utilization of IL-F not only leads to secondary mesopores in hierarchical TiO_2 microspheres, but also significantly increases the specific surface area and produces oxygen vacancies. Our results show that HDM-TiO_2 enhances the photocatalytic activity on degradation of MB and acetone, and also presents a high performance on lithium storage. Therefore, this work provides a promising way to introduce secondary mesopores in hierarchically mesoporous TiO_2 by ionic liquids and gives new insights for the design of hierarchically dual-mesoporous TiO_2 with nanoscale defects and an enhanced photocatalytic activity and lithium storage

Experimental Section

Chemicals

Diethylenetriamine (DETA) (99%), titanium isopropoxide (TTIP) (95%), propanol (95%) and acetone (98%) (GC) were provided by Shanghai Aladdin Biochemical Technology Co, Ltd. 1-butyl-3-methylimidazolium tetrafluoroborate [BMIm][BF$_4$] (≥99%) was provided by Lanzhou Greenchem ILs. All chemical reagents were utilized as received without further purification and distilled water was used in the whole experiment

Synthesis

In a typical procedure, 24 μL DETA and 1 mL [BMIm] [BF$_4$] were mixed with 35 mL propanol in a 50 mL sealed Teflon-lined stainless steel autoclave. After stirring for ten minutes, 2 mL TTIP was added to the mixed solution. After stirring for another 10 minutes, the autoclave was placed in a bake oven and kept at 180 °C for 24 h. After cooling to room temperature, the sample was obtained through centrifugal separation, washed three times with water and ethanol respectively, and dried at 70 °C for 12 h. The dried sample was finally calcined at 600 °C in air for 4 h to obtain hierarchically dual-mesoporous TiO_2 microspheres (HDM-TiO_2). The [BMIm][BF$_4$] was replaced by water to synthesize hierarchically TiO_2 microspheres (HM-TiO_2) for comparison

Characterization

The sample morphology was performed in a field emission scanning electron microscope (Hitachi S-4800, 5 kV) and a transmission electron microscope (TEM, JEOL-2100F). Phase identification and crystal size were determined by X-ray diffraction (D8 ADVANCE XRD) patterns with Cu Kα radiation operated at a tube current of 40 mA and a voltage of 40 kV at a scan rate of 0.1 degree (2θ) s^{-1}. Data varying from 10° to 80° was collected. SAXS patterns were measured by SAXSess mc2 (Anton Paar) apparatus, equipped with a Cu tube (λ = 1.54 Å) operating at 40 kV and 50 mA. The BET specific surface area was measured by N$_2$ adsorption (TriStar TM II 3020). The measurement began after the samples were degassed at 120 °C for 12 h. Ultraviolet-visible spectroscopy diffuse reflectance spectra (UV-vis DRS) were obtained by a UV-vis spectrophotometer (UV-2550). X-Ray photoelectron spectroscopy (XPS) was taken on a PHI5000 Versa Probe system with monochromatic Al Kα X-rays to determine the surface elements, composition and chemical state of the samples. Fourier transform infrared spectra (FT-IR) of the samples were applied on a Nicolet Avatar 360 FT-IR infrared spectrometer by using conventional KBr pellets. The photoluminescence spectra (PL) were obtained by LS55 (PERKIN-ELMER) with an excitation wavelength of 320 nm. Electron paramagnetic resonance (EPR) spectra were measured by an EMX 10/12 spectrometer working in the X-band at room temperature with an EPR quartz probe cell. Raman spectra were applied on an Invia Raman Microscope with 632.8 nm laser as the excitation source under ambient conditions. Thermogravimetric analysis (TGA) was obtained under an air flow with an up rate of 5 °C min^{-1}.

Photocatalytic activity Evaluation

Methylene blue (MB) was chosen as model pollutant to conduct photocatalytic activity tests. Typically, 100 mL 0.02 mg/mL MB solution and 20 mg catalyst were displayed in a beaker, the distance between the solution and a 300 W xenon lamp (PLS-SXE300C, Beijing Trusttech Co., Ltd.) with a 200-800 nm UV lamp was fixed at 10 cm. The solution was stirred in the dark for 30 minutes until the concentration of MB remained unchanged, indicating that the adsorption of MB is saturated. During the photocatalytic reaction, 2 mL suspension was taken out every 2.5 minutes. The catalyst in the suspension was removed by centrifugation. The remaining pure liquid was tested by UV-vis spectroscopy. In order to test the vapor-phase catalysis of the samples, acetone was chosen as the pollutant to detect the performance of the samples. In a typical experiment, 10 mg photocatalysts were added to 2 mL ethanol in a glass reactor, then the mixed solution was sonicated for 30 minutes to get a suspension and dried in 80 °C for 12 h. The catalysts were deposited on the bottom of the reactor to form thin films. The reactor was put into a sealed vessel, and then 5 uL acetone was added to the sealed vessel through an injection valve to form an initial concentration of 600 ppm. It was kept for 30 minutes to balance the concentration of acetone. Then a 300 W, 200-800 nm UV lamp (2 cm above the dishes) (Perfect Light PLS-SXE 300) was opened in the reactor. Every 10 minutes 100 uL gas was obtained from the system by using a syringe and analyzed the gas with a gas chromatograph (GAS CHROMATOGREPH GC 900C).

Lithium storage

The lithium storage measurements were carried out by using two-electrode Swagelok cells and regarding lithium metal as the reference electrode and the counter electrode. The working electrode was made up of active material (e.g., HDM-TiO_2), a conductive agent (carbon black, Super-P-Li) and a polymer binder [poly (vinylidene difluoride), PVDF, Aldrich] in a weight ratio of 70:20:10. The electrolyte was 1.0 M LiPF$_6$ in a 50:50 (w/w) mixture of ethylene carbonate and diethyl carbonate. Cell assembly was obtained in an Ar-filled glovebox under a 1.0 ppm concentration of moisture and oxygen. Cyclic voltammetry (1-3 V, 0.2 mV/s) was performed by using an electrochemical workstation (CHI 660C). The charge/discharge tests were obtained by using a NEWARE battery tester at different current rates (1 C) (170 mA g^{-1}) with a voltage range of 1-3 V. Electrochemical impedance spectra (EIS) were performed on an electrochemical workstation (Autolab PGSTAT302N) in the frequency range from 100 kHz to 0.01 Hz with an amplitude of 5 mV. All the electrochemical measurements were carried out at room temperature.

Photocurrent Measurements

Photocurrent measurements were performed by using a Pt foil as the counter electrode and a Ag/AgCl reference electrode at a 0.5 V potential bias on a CHI 660D electrochemical workstation (Chenhua Instrument, Shanghai, China) under a 300 W, 200-800 nm UV lamp (2 cm above the dishes) (Perfect Light FX 300) in a conventional three-electrode system. Catalysts (5 mg) and Nafion solution (100 μL, 0.5 wt%) were firstly dispersed in a mixed solvent of water/ethanol (1 mL, 1:1 v/v) and sonicated at least 30 minutes to form a homogeneous ink (The working

FULL PAPER

electrodes). The working electrode was obtained by drop-casting the above ink (50 µL) onto FTO glass with an area of 1 cm^2

Conflict of interest

The authors declare no conflict of interest

[1] E.-J.-W. Crossland, N. Noel, V. Sivaram, T. Leijtens, J.-A.-A. Webber and H. J. Snaith, *Nature* **2013**, *495*, 215-219.

[2] X.-Y. Yang, L. Alexandre, L. Arnaud, G. Tian, B.-L. Su, *Chem. Commun.* **2011**, *47*, 2763-2786.

[3] X.-H. Li, J. Lian, M. Lin and Y.-T. Chan, *J. Am. Chem. Soc.* **2011**, *133*, 672-675.

[4] X.-F. Li, T.-X. Fan, H. Zhou, S.-K. Chow, W. Zhang, D. Zhang, Q.-X. Guo and H. Ogawa, *Adv. Funct. Mater.* **2009**, *19*, 45-56.

[5] Y. Lu, X. Cheng, G. Tian, H. Zhao, L. He, J. Hu, S.-M. Wu, Y. Dong, G.-G. Chang, S. Lenaerts, S. Siffert, G. Van Tendeloo, Z.-F. Li, L.-L. Xu, X.-Y. Yang and B.-L. Su, *Nano Energy* **2018**, *47*, 8–17.

[6] J.-C. Rooke, T. Barakat, M.-F. Finol, P. Billemont, G. De Weireld, Y. Li, Y, R. Cousin, J.-M. Giraudon, S. Siffert and J.-F. Lamonier, *Appl. Catal. B Environ.* **2013**, *142*, 149-160.

[7] Y. Gao, B.-F. Fan, R. Feng, C.-L. Ye, X.-J. Wei, J. Liu and X.-H. Bu, *Nano Energy* **2017**, *40*, 462−470.

[8] S.-Y. Gao and K.-R. Geng, *Nano Energy* **2014**, *6*, 44−50.

[9] Z.-K. Zheng, B.-B. Huang, J.-J. Lu, X.-Y. Qin, X.-Y. Zhang and Y. Dai, *Chem-Eur J.* **2012** *17*, 15032-15038.

[10] Y. Dong, .S.-Y. Chen, Y. Lu, Y.-X. Xiao, J. Hu, S.-M. Wu, Z. Deng, G.Tian, G.-G. Chang, J. Li, S, Lenaerts, C. Janiak, X.-Y. Yang and B.-L. Su, *Chem-Asian J.* DOI: 10.1002/asia.201800359

[11] C.-P. Han, D. Yang, Y.-K. Yang, B.-B. Jiang, Y.-J. He, M.-Y. Wang, A.-Y. Song, Y.-B. He, B.-H. Li and Z.-Q. Lin, *J. Mater. Chem. A*, **2015**, *3*, 13340-13349.

[12] J. Wang and Z.-Q. Lin, *Chem-Asian J.* **2012**, *7*, 2754-2762.

[13] X.-Y. Li, L.-H. Chen, Y. Li, J.-C. Rooke, C. Wang, Y. Lu, A. Krief, X.-Y.Yang and B.-L. Su, *J. Colliod Interf. SCI.* **2012**, *368*, 128-138

[14] Y. Li, S. Wang, Y.-B. He, L.-K. Tang, Y. V. Kaneti, W. Lv, Z.-Q. Lin, B.-H. Li, Q.-H. Yang and F.-Y. Kang, *J. Mater. Chem. A* **2017**, *5*, 4359-4367.

[15] X. Lu, F. Huang, X. Mou, Y. Wang and F. Xu, *Adv. Mater.* **2010**, *22*, 3719-3722.

[16] L.-H. Chen, X.-Y. Li, G. Tian, Y. Li, H.-Y. Tan, G.-V. Tendeloo, G.-S. Zhu, S.-L. Qiu, X.-Y. Yang and B.-L. Su, *Chemsuschem* **2011**, *4*, 1452-1456.

[17] X.-Y. Yang, S.-B. Zhang, Z.-M. Qiu, G. Tian, Y.-F. Feng, and F.-S. Xiao, *J. Phys. Chem. B*, **2004**, 108, 4696–4700.

[18] D. Wu, Y. Wang, H. Dong, F. Zhu, S. Gao, K. Jiang, L. Fu, J. Zhang and D. Xu, *Nanoscale* **2013**, *5*, 324-330.

[19] W.-Q. Fang, J.-Z. Zhou, J. Liu, Z.-G. Chen, C. Yang, C.-H. Sun, G.-R. Qian, J. Zou, S.-Z. Qiao and H.-G. Yang, *Chem-Eur J.* **2011**, *17*, 1423-1427.

[20] J. S. Chen, Y.-L. Tan, C.-M. Li, Y.-L. Cheah, S. Madhavi, F.-Y.-C. Boey, L. A. Archer and X. W. Lou, *J. Am. Chem. Soc.* **2010**, *132*, 6124-6130.

[21] Z.-K. Zheng, B.-B. Huang, X.-Y. Qin, X.-Y. Zhang and Y. Dai, *Chem-Eur J.* **2010**, *16*, 11266-11270.

[22] B.-S. Li, B.-J. Xi, Z.-Y. Feng, Y. Lin, J.-C. Liu, J.-K. Feng, Y.-T. Qian and S.-L. Xiong, *Adv. Mater.* **2018**, *30*, 1705788.

[23] M.-Z.Ge, J.-S. Cai, James Iocozzi, C.-y. Cao, J.-Y. Huang, X.-N. Zhang, J.-L. Shen, S.-C. Wang, S.-N. Zhang, K.-Q. Zhang, Y.-K. Lai and Z.-Q. Lin, *Int. J. Hydrogen Energ.* **2017**, *42*, 8418-8449.

[24] M.-Y. Wang, J. Ioccozia, L. Sun, C.-J. Lin and Z.-Q. Lin, *Energy Environ. Sci.* **2014**, *7*, 2182-2202.

[25] M. D'Arienzo, J. Carbajo, A. Bahamonde, S. Polizzi, R. Scotti, L. Wahba and F. Morazzoni, *J. Am. Chem. Soc.* **2011**, *133*, 17652-17661.

[26] H.-G. Yang, C.-H. Sun, S.-Z. Qiao, J. Zou, G. Liu, S.-C. Smith, H.-M. Cheng and G.-Q. Lu, *Nature* **2008**, *453*, 638-641.

[27] X.-Y. Pan, M.-Q. Yang, X.-Z. Fu, N. Zhang and Y.-J. Xu, *Nanoscale* **2012**, *4*, 6682-6691.

[28] S.-M. Wu, X.-L. Liu, X.-L. Lian, G. Tian, C. Janiak, Y.-X. Zhang, Y. Lu, H.-Z. Yu, J. Hu, H. Wei, H. Zhao, G.-G. Chang, G.-V. Tendeloo, L.-Y. Wang, X.-Y. Yang and B.-L. Su, Adv. Mater. DOI: 10.1002/adma.201802173.

[29] X.-Y. Yang, S.-B. Zhang, Z.-M. Qiu, G. Tian, Y.-F. Feng and F.-S. Xiao, *J. Phys. Chem. B.* **2004**, *108*, 4696-4700.

[30] D. Nakamura, I. Gunjishima, S. Yamaguchi, T. Ito, A. Okamoto, H. Kondo, S. Onda and K. Takatori, *Nature* **2004**, *430*, 1009-1012.

[31] X.-Y. Yang, L.-H. Chen, Y. Li, J. C. Rooke, C. Sanchez, B.-L. Su, *Chem. Soc. Rev.* **2017**, *46*, 481-558.

[32] X.-Y. Yang, Y. Li, L. Arnaud, J.-G. Yu, B.-L. Su, *Pure Appl. Chem.* **2009**, *81*, 65-2307.

[33] D. Chen, L. Cao, F. Huang, P. Imperia, Y.-B. Cheng and R. A. Caruso, *J. Am. Chem. Soc.* **2010**, *132*, 4438-4444.

[34] R.-Li Liu, Y.-F. Shi, Y. Wan, Y. Meng, F.-Q. Zhang, D. Gu, Z.-X. Chen, B. Tu and D.-Y. Zhao, *J. Am. Chem. Soc.* **2006**, *128*, 11652-11662.

[35] Y.-Y. Wen, H.-M. Ding and Y.-K. Shan, *Nanoscale* **2011**, *3*, 4411-4417.

[36] Y. Chen, W. Li, J. Wang, Y. Gan, L. Liu and M. Ju, *Appl. Catal. B Environ.* **2016**, *191*, 94-105.

[37] S. Wang, L. Pan, J. J. Song, W. Mi, J. J. Zou, L. Wang and X. Zhang, *J. Am. Chem. Soc.* **2015**, *137*, 2975-2983.

[38] M. A. Rahman, S. Bazargan, S. Srivastava, X. Wang, M. Abd-Ellah, J. P. Thomas, N. F. Heinig, D. Pradhan and K. T. Leung, *Energy Environ. Sci.* **2015**, *8*, 3363-3373.

FULL PAPER

Entry for the Table of Contents

FULL PAPER

Hierarchically dual-mesoporous TiO_2 has been synthesized using co-templating, and its mesostructured defects caused by ion liquid lead a high-level of the oxygen vacancies, which not only significantly enhance photo-electro performance. The mechanism our proposed provides a better understanding with the role of hierarchical mesoporosity for enhancing the molecular diffusion, ion transportation and electron transformation.
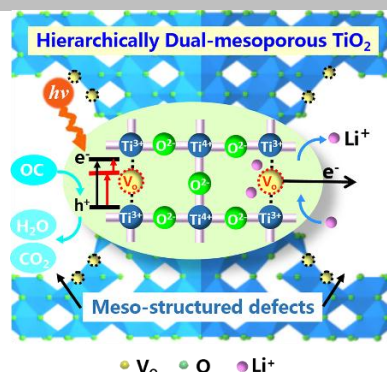
Sa Xiao, Yi Lu, Xin Li, Bing-Yu Xiao, Liang Wu, Jian-Ping Song, Yu-Xuan Xiao, Si-Ming Wu, Jie Hu, Yong Wang, Gang-Gang Chang, Ge Tian,* Silvia Lenaerts, Christoph Janiak, Xiao-Yu Yang* and Bao-Lian Su

Page No. – Page No.

Hierarchically Dual-mesoporous TiO_2 Microspheres for Enhanced Photocatalytic Properties and Lithium Storage